Nano Research

Open Access

Research Article

Inkjet-printed carbon nanotube-MoS_2 heterojunction p-n diodes

Fugu Tian[1], Dingzhou Cui[1], Mingrui Chen[2], Zhiyuan Zhao[2], Wenbo Chen[1], Zikuan Wang[1], Silvia Guadagnini[3], Sarah Alsaggaf[4,5], Shahad Albawardi[4,5], Michelle L. Povinelli[1,3], Moh R. Amer[1,4,5] ✉, Jia Grace Lu[1,3], and Chongwu Zhou[1] ✉

[1] *Ming Hsieh Department of Electrical and Computer Engineering, University of Southern California, Los Angeles, CA 90089, USA*
[2] *Mork Family Department of Chemical Engineering and Materials Science, University of Southern California, Los Angeles, CA 90089, USA*
[3] *Department of Physics & Astronomy, Dornsife College of Letters, Arts, & Sciences, University of Southern California, Los Angeles, CA 90089, USA*
[4] *Center of Excellence for Green Nanotechnologies, King Abdulaziz City for Science and Technology, Riyadh 12354, Saudi Arabia*
[5] *Microelectronics and Semiconductor Institute, King Abdulaziz City for Science and Technology, Riyadh 12354, Saudi Arabia*

Cite this article: *Nano Research*, **2025**, *18*, 94907059. https://doi.org/10.26599/NR.2025.94907059

ABSTRACT: The p-n junction diode and field-effect transistor are foundational elements in modern electronics and optoelectronics. While high-performance field-effect devices have been realized using monolayered materials and their heterostructures, there has been a notable absence of p-n heterojunction diodes derived from inkjet-printed two-dimensional (2D) materials, which may lead to the development of complex electronic and optoelectronic circuits. This study addresses this gap by detailing the development and characterization of heterojunction p-n diodes fabricated through the inkjet printing of carbon nanotubes (CNTs) and molybdenum disulfide (MoS_2). The use of inkjet printing technology for both CNTs and MoS_2 allows for precise, scalable, and cost-effective fabrication. The resulting heterojunction diodes exhibit excellent diode behavior, with a rectification ratio exceeding 10^3. Additionally, the diode shows significant photoconductive properties, with a rapid photoresponse time of approximately 2 μs. This swift photoresponse is essential for high-speed optoelectronic applications, making the diode a promising component in advanced electronic systems. The study underscores the potential of inkjet printing technology to revolutionize the production of sophisticated, low-cost electronic devices with superior performance metrics, particularly in terms of photoresponse efficiency and speed. The integration of CNTs and MoS_2 via inkjet printing not only streamlines the manufacturing process but also enhances the functional properties of the heterojunction diodes, positioning it as a viable candidate for future optoelectronic applications.

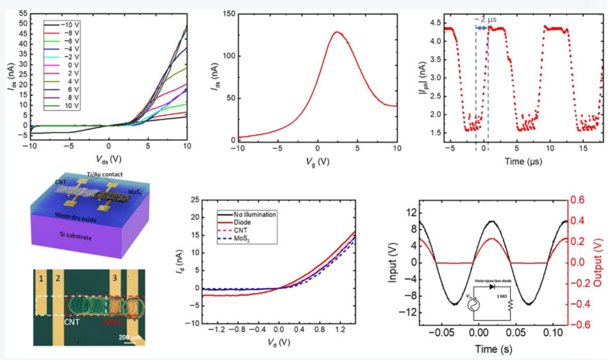

KEYWORDS: carbon nanotube (CNT), MoS_2, heterojunction p-n diode, photo response, inkjet printing

1 Introduction

The rapid evolution of modern electronics and optoelectronics has been largely driven by two fundamental components: the p-n junction diode and the field-effect transistor [1–6]. These devices are integral to a wide range of applications, from basic electronic circuits to complex photodetectors and communication systems [7–10]. The ongoing miniaturization and performance enhancement of these components are essential to keep pace with the ever-increasing demands for faster, more efficient, and more versatile electronic systems [11–14].

In recent years, the exploration of reduced-dimensionality materials, such as monolayered semiconductors and carbon-based nanostructures, has opened new avenues for scaling down these components to atomic thicknesses [15–19]. These materials offer exceptional electrical, mechanical, and optical properties that are not attainable with traditional bulk materials. High-performance field-effect transistors (FETs) have been successfully fabricated using monolayered materials, showcasing remarkable performance such as high carrier mobility and excellent on/off ratios [20–23]. However, the development of a p-n heterojunction diode derived from these ultrathin materials remained a challenge in the field of

Received: July 28, 2024; **Revised:** September 12, 2024
Accepted: October 2, 2024

✉Address correspondence to Chongwu Zhou, chongwuz@usc.edu; Moh R. Amer, mamer@kacst.edu.sa

complex, integrated electronic and optoelectronic circuits that require both FETs and diodes to function effectively, until Mark C. Hersam and his team successfully fabricated such devices using advanced techniques such as atomic layer deposition and precise material transfer methods [3].

Moreover, traditional thin film two-dimensional (2D) material deposition methods such as spin-coating necessitate additional patterning and etching steps, which substantially increase the complexity and cost of device fabrication. In contrast, inkjet printing offers a lithography-free, drop-on-demand deposition method. This technique allows for the direct "writing" of 2D material inks onto the desired locations with computer assistance, making it highly compatible with 2D inks [24, 25]. Compared to colloidal quantum dots, which also offer a cost-effective fabrication approach but often require complex processing steps, inkjet-printed carbon nanotubes (CNTs) provide a more straightforward and versatile solution [26]. However, to date, the literature contains only a limited number of demonstrations of inkjet-printed 2D FET devices. Furthermore, the performance metrics of these reported inkjet-printed 2D FETs have generally been suboptimal [27, 28].

Addressing this gap, our study focuses on the innovative use of inkjet printing technology to fabricate a heterojunction p-n diode using single-walled CNTs (SWCNTs) and molybdenum disulfide (MoS_2). Inkjet printing offers a versatile, scalable, and cost-effective approach to depositing these materials with high precision [25]. This method not only simplifies the fabrication process but also allows for the creation of intricate device architectures that are difficult to achieve with conventional techniques.

The resulting heterojunction diode exhibits robust diode behavior, characterized by a relatively high rectification ratio, which is crucial in electronic circuits. Moreover, the device demonstrates significant photoconductive properties, with a photoresponse time of approximately 2 μs, indicating its potential for high-speed optoelectronic applications. These attributes highlight the diode's suitability for integration into advanced electronic systems where rapid photoresponse and high rectification ratio are critical [29–31].

In this paper, we present a comprehensive analysis of the fabrication process, device characterization, and performance metrics of the inkjet-printed SWCNT-MoS_2 heterojunction p-n diodes. Our findings underscore the potential of inkjet printing technology to revolutionize the production of low-cost, high-performance electronic devices, paving the way for future advancements in optoelectronic applications [32–34].

2 Experimental

2.1 MoS_2 and CNT ink preparation

The electrochemical exfoliation of MoS_2 was conducted in a two-electrode cell. A MoS_2 crystal (SPI Supplies) served as the cathode was fixed with a copper clip, while a graphite rod was used as the anode. The electrolyte consisted of 10 mg/mL tetraheptylammonium bromide (THAB) (99%, Sigma-Aldrich) in acetonitrile. During exfoliation, tetraheptylammonium (THA^+) cations were intercalated between MoS_2 layers under an 8 V applied voltage for 1 h.

After intercalation, the exfoliated MoS_2 was rinsed with ethanol to remove residual acetonitrile and THAB, then transferred to a 25 mg/mL polyvinylpyrrolidone (PVP, M.W. 58,000, Alfa Aesar) solution in dimethylformamide (DMF). Bath sonication for 2 h produced a greenish MoS_2 dispersion. Additionally, recent studies have demonstrated alternative methods for producing 2D MoS_2 in large quantities at lower costs, further enhancing the scalability of this material [35, 36].

To eliminate excess PVP, the dispersion was washed four times with isopropanol (IPA). Centrifugation at 9000 rpm isolated the MoS_2 nanoplates, which were then redispersed in IPA. A subsequent centrifugation at 1500 rpm for 5 min removed larger aggregates. To improve ink spreading and drying on substrates, 10 vol.% 2-butanol was added to the final MoS_2 dispersion [27].

The semiconducting SWCNTs ink (0.01 mg, 99.9%, NanoIntegris) was diluted in toluene to a final concentration of 0.00125 mg/mL. The resulting solution underwent bath sonication for 2 h, yielding a homogenous brown CNT dispersion.

2.2 Inkjet printing and post-processing of printed heterojunction

The substrates were initially immersed in poly-L-Lysine (Sigma-Aldrich) to mitigate the coffee ring effect and ensure a homogeneous pattern. Excess solution was removed by rinsing the samples with deionized (DI) water. The CNT ink was then printed onto Si/SiO_2 (300 nm) or polyimide substrates using an inkjet printer (Microplotter Desktop, SonoPlot, Inc.). The ink film was directly deposited onto prefabricated Ti/Au (5/50 nm) source/drain electrodes, which had been patterned via lithography and deposited using electron beam evaporation. After printing, the sample was immersed in toluene for 3 s, followed by sequential washing with acetone and IPA.

Following a second immersion in poly-L-Lysine and subsequent DI water rinse, the MoS_2 ink was printed using the same procedure as the CNT ink. To remove PVP and other compounds from the ink preparation, the devices were immersed in a 10 mg/mL solution of bis(trifluoromethane)sulfonimide (TFSI, > 95.0%, Sigma-Aldrich) in 1,2-dichloroethane (Sigma-Aldrich) at 80 °C for 1 h. Finally, an annealing treatment was conducted in an argon atmosphere at 200 °C for 1 h.

2.3 Device characterization

Scanning electron microscopy (SEM) was conducted using a Nova NanoSEM 450 field-emission scanning electron microscopy. Optical microscopy images and Raman mapping spectra were obtained with a confocal Raman spectroscopy (Renishaw).

The electrical characteristics of the printed heterojunction diode were measured in a vacuum chamber probe station (Lakeshore CPX-VF) using a Keysight B1500A parameter analyzer. Photoresponse measurements were performed using a Keithley 4200-SCS semiconductor characterization system. For the focused beam measurements, a HL6312G laser diode (635 nm) from Thorlabs was employed, while a CT80AAA solar simulator from Photo Emission Tech., Inc. was used for global illumination experiments. The response time of the photoconduction measurement was assessed using a Rigol DHO914 oscilloscope in conjunction with a low-noise preamplifier SR560.

3 Results and discussion

The development of heterostructure diodes has been a focal point in the advancement of modern electronic and optoelectronic devices. Heterostructure diodes, which consist of interfaces between different semiconductor materials, offer unique electronic and optical properties that are not available in homojunction counterparts [37, 38]. These properties arise from the distinct band alignments and charge transport mechanisms at the heterojunction interface, enabling superior performance in terms of charge carrier separation, mobility, and recombination rates [39, 40]. Specifically, heterostructure p-n diodes have garnered significant attention due to their potential applications in photovoltaics, light-emitting diodes, and photodetectors. The strategic combination of materials such as CNTs and MoS_2 leverages their complementary electrical and optical properties [3]. CNTs, with their excellent electrical conductivity and mechanical strength [18, 41, 42] and MoS_2, known for its high electron mobility and direct bandgap in monolayer form [21, 43, 44], create an ideal platform for developing high-performance heterojunction devices.

3.1 Device characterization of CNT/MoS_2 heterojunction p-n diode

Figure 1(a) presents a schematic illustration of our SWCNTs (p-type) and MoS_2 (n-type) heterojunction p-n diode. To verify the individual p-type and n-type behaviors of CNTs and MoS_2, a four-probe electrode structure was utilized, providing a comprehensive understanding of each component's function within the device. The source and drain electrodes were patterned through lithography, followed by the deposition of 5 nm of Ti and 50 nm of Au using electron-beam evaporation. Subsequently, MoS_2 ink with a concentration of 0.4 and 0.00125 mg/mL CNT ink was inkjet-printed onto the channel region using the SonoPlot Microplotter system. This system operates by lowering the printing nozzle to bring the ink into contact with the substrate, forming a circular ink film with a diameter of 400 μm, which was optimized for heterojunction diode performance rather than the finest resolution possible. The nozzle is then moved horizontally to pattern the ink film. Typically, two to three printing passes are needed to achieve a continuous and uniform film. While our setup focused on the specific performance characteristics of the device, inkjet printing can achieve much smaller feature sizes, with resolutions down to 20–50 μm depending on the substrate and ink properties. The thickness of the printed films generally ranges from 10 to 60 nm, with statistical measurements showing a standard deviation of approximately ±5%, indicating uniformity across samples. These measurements were validated using atomic force microscopy (AFM) and profilometry, ensuring consistent thickness across the printed areas [27]. Figure 1(b) shows the optical microscopy image of the fabricated device. The MoS_2 region, delineated by a red dashed line, is visible as a light green area against the SiO_2 oxide layer background. In contrast, the CNT region, outlined by a white

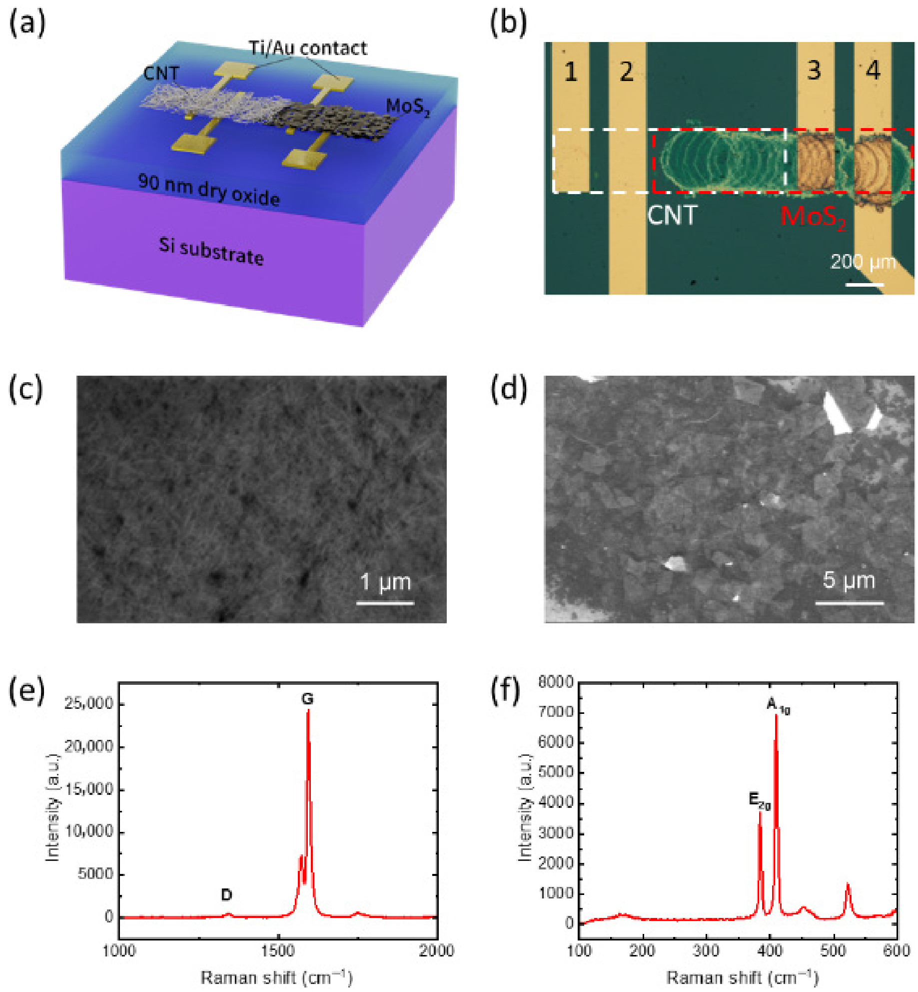

Figure 1 Characterization of the heterostructure p-n diode. (a) Schematic diagram of the CNT-MoS_2 heterostructure p-n diode with a four-probe electrode structure. (b) Optical microscopy image of the fabricated device, with CNT and MoS_2 regions outlined by white and red dashed lines, respectively. The CNT region appears nearly transparent and invisible under the microscopy. (c) and (d) SEM images of the CNT and MoS_2 regions on the device. (e) Raman spectra of CNT, displaying the G band (in-plane bond stretching mode of the C–C bonds in the hexagonal lattice) at 1685 cm^{-1} and the defect-induced peak (D band) at 1350 cm^{-1} [45]. (f) Raman spectra of MoS_2, featuring two characteristic bands: the E_{2g} band (in-plane vibrations) at 385 cm^{-1} and the A_{1g} band (out-of-plane vibrations) at 408 cm^{-1} [46].

dashed line, is nearly invisible under the microscopy. In this structure, electrodes 1 and 2 were employed to measure the electrical properties of the CNT segment, electrodes 3 and 4 for the MoS_2 segment, and electrodes 2 and 3 to evaluate the heterojunction diode behavior. To more precisely characterize these regions, SEM and Raman spectroscopy were employed. Figures 1(c) and 1(e) display the SEM and Raman spectra of the CNT, respectively, while Figs. 1(d) and 1(f) present the corresponding analyses for the MoS_2 region. Given that the entire diode was fabricated via inkjet printing, minor peaks observed in the Raman spectra may be attributed to residual ink solution. The methods section provides further details on the device fabrication.

3.2 Gate-dependent electrical properties of the device

With the help of the four-electrode pattern, the CNT part and MoS_2 part can be measured separately and with ease. Some hysteresis is observed in the I_{ds}–V_g curve of the CNT region when measured in ambient air; however, it does not significantly affect the I_{ds}–V_{ds} characteristics. To provide better characterization of intrinsic behavior, all *I*–*V* characteristic measurements are conducted in a vacuum chamber to eliminate the influence of oxygen and moisture, thereby preventing potential degradation of CNT and MoS_2 due to Joule heating during the measurement. As illustrated in Figs. 2(a) and 2(c), the I_{ds}–V_{ds} characteristics of the CNT region (between electrode 1 and 2) and MoS_2 region (between electrode 3 and 4) exhibit typical p-type and n-type material behaviors, respectively. The curves demonstrate current saturation at negative voltage bias for the p-type CNT and at positive voltage bias for the n-type MoS_2 [47, 48], consistent with the expected electrical properties of p-channel and n-channel metal-oxide-semiconductor field-effect transistors (MOSFETs).

Figures 2(b) and 2(d) present the I_{ds}–V_g characteristics of the device under a drain-source voltage bias (V_{ds}) of 6 V. These plots confirm the p-type behavior of the CNT region and the n-type behavior of the MoS_2 region. Specifically, in the I_{ds}–V_g curve for the CNT, the drain current decreases as the gate voltage becomes more positive, indicative of p-type behavior. Conversely, in the I_{ds}–V_g curve for the MoS_2, the drain current increases as the gate voltage becomes more positive, characteristic of n-type behavior. These observations verify that the CNT and MoS_2 materials maintain their p-type and n-type properties within the heterostructure device configuration.

Figure 3(a) shows the I_{ds}–V_g characteristic of the heterojunction, which displays typical antiambipolar behavior [3, 49, 50]. In an antiambipolar device, the current increases as the gate voltage moves from one extreme towards an intermediate value, reaches a maximum, and then decreases as the gate voltage continues towards the opposite extreme. This behavior occurs in heterojunctions combining materials with different conduction mechanisms, such as n-type and p-type materials. At specific gate voltages, one type of charge carrier (electrons or holes) predominates, but as the voltage changes, the balance shifts, resulting in a peak in the current. The device transitions from nearly insulating behavior at V_g = −10 V to a poorly rectifying state at V_g = 2 V, and to a highly rectifying diode at V_g = 10 V. Figure 3(a) shows the I_{ds}–V_g curve of the heterojunction region, with a noticeable peak around 2.5 V. As illustrated in Fig. 3(b), the junction region exhibits diode behavior under various gate biases, with the threshold voltage decreasing as the gate voltage increases. Figure 3(c) provides a zoomed-in view of the I_{ds}–V_g curve for V_g ranging from −10 to −5 V, where the device is dominated by the n-type MoS_2. In contrast, Fig. 3(d) focuses on the V_g ranging from 5 to 10 V, where the p-type CNT predominates.

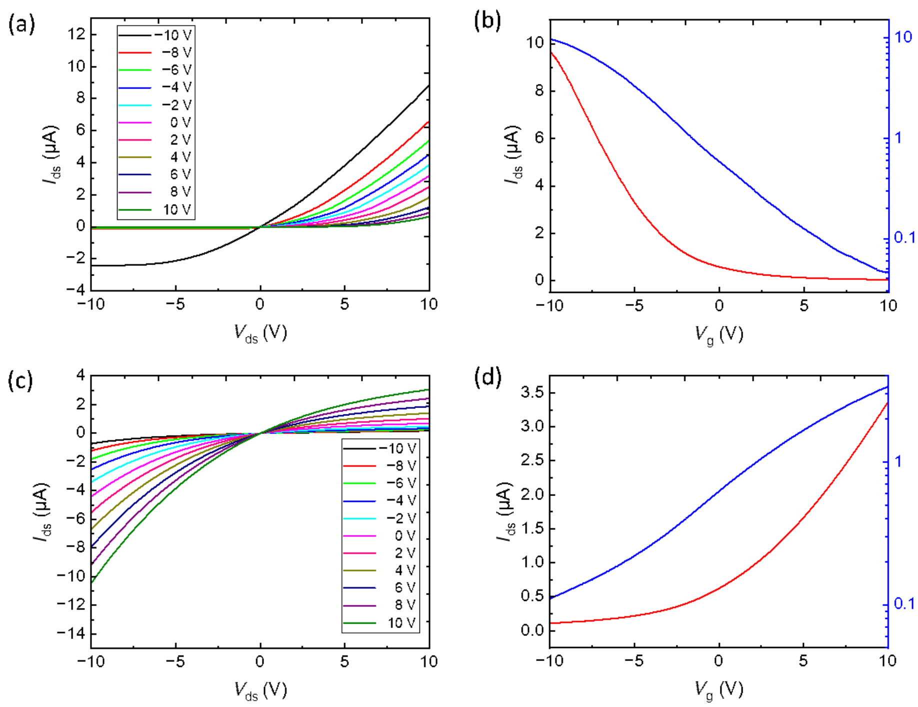

Figure 2 Electrical characterization of the CNT and MoS_2 regions. (a) I_{ds}–V_{ds} curve for the CNT region, with gate bias varying form −10 to 10 V, showing typical p-type behavior with current saturation occurring at negative voltage bias. (b) I_{ds}–V_g curve for the CNT region under a V_{ds} of 6 V, with logarithm scale in blue on the right, confirming p-type behavior with the drain current decreasing as the gate voltage becomes more positive. (c) I_{ds}–V_{ds} curve for the MoS_2 region, with gate bias varying form −10 to 10 V, exhibiting typical n-type behavior with current saturation at positive voltage bias. (d) I_{ds}–V_g curve for the MoS_2 region under a V_{ds} of 6 V, with logarithm scale in blue on the right, confirming n-type behavior with the drain current increasing as the gate voltage becomes more positive. These characteristics validate the preservation of intrinsic p-type and n-type properties in the CNT and MoS_2 regions, respectively.

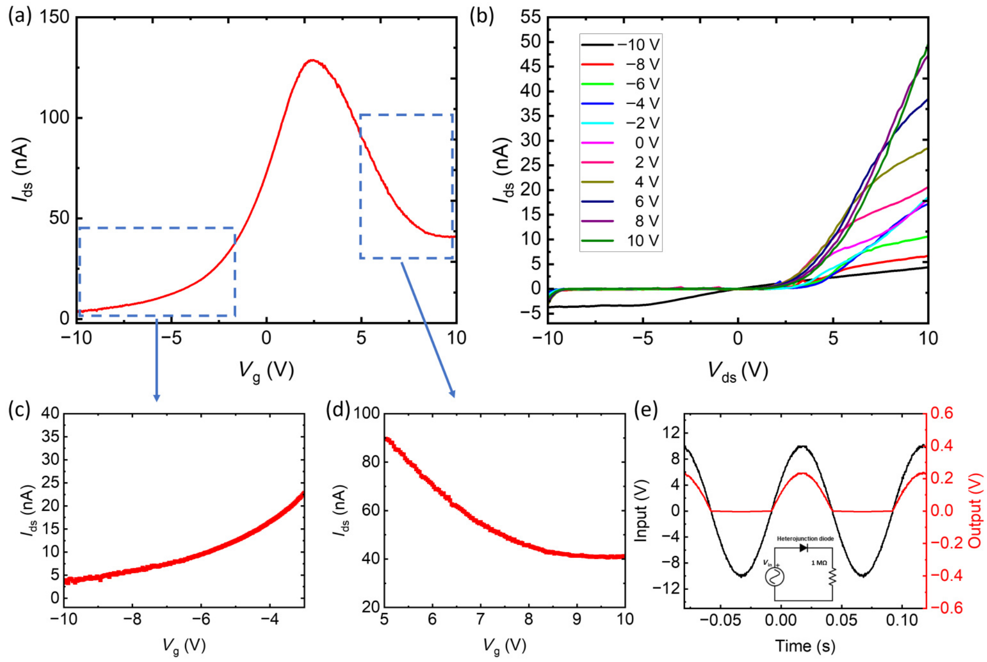

Figure 3 Electrical characterization of the heterojunction diode. (a) I_{ds}–V_g characteristics of the heterojunction at V_{ds} = 6 V, displaying typical antiambipolar behavior. The current increases as the gate voltage moves from one extreme towards an intermediate value, reaches a maximum, and then decreases as the gate voltage continues towards the opposite extreme. (b) I_{ds}–V_{ds} characteristics of the junction region, demonstrating ideal diode behavior under various gate biases, with a decreasing threshold voltage as the gate voltage increases. (c) Zoomed-in I_{ds}–V_g curve for V_g ranging from −10 to −5 V, where the device is dominated by the n-type MoS_2. (d) Zoomed-in I_{ds}–V_g curve for V_g ranging from 5 to 10 V, where the device is dominated by the p-type CNT. (e) Measurement of the rectifying ratio using a half-wave rectifying circuit with a 1 MΩ load resistance, demonstrating a rectifying ratio of approximately 10^3 at zero gate bias, which is relatively high compared to most heterostructure devices.

The rectifying ratio was measured to characterize the diode behavior of the device. This measurement was conducted using a typical half-wave rectifying circuit with a 1 MΩ load resistance. Data acquisition was performed using an oscilloscope, and the sinusoidal signal was generated by a function generator. By calculating the ratio of forward current ($I_{forward}$) to reverse current ($I_{backward}$) at the positive and negative peak values of the signal, the rectifying ratio was determined to be approximately 10^3 at zero gate bias. This value is comparatively high when evaluated against most heterostructure devices.

3.3 Photoconduction effect and response time measurement in ambient air

To further investigate the device's application potential, photoconduction measurements were performed at zero gate bias. As shown in Fig. 4(a), when illuminated by a solar simulator, the heterojunction diode exhibits a pronounced photocurrent in the negative bias region, indicating its potential use as a photodetector [51]. To confirm that the photoconduction current originates from the junction area, a 635 nm red laser beam was focused on different parts of the device. Figure 4(b) demonstrates that when the laser beam is focused on either the CNT or MoS_2 regions alone, there is no significant photoresponse compared to no illumination. This finding indicates that the observed photoconduction current under global illumination originates from the junction area rather than from the individual semiconductor components.

Additionally, the potential contribution of thermal effects due to uniform global illumination or a focused beam was considered. Illumination could induce temperature changes in the sample, which may impact the carrier density and influence the resulting photocurrent. To distinguish the influence of thermal effects from photoconductive mechanisms, a power dependence measurement under uniform solar simulator illumination was performed. As shown in Fig. 4(c), the negative bias region exhibited a clear linear relationship between photocurrent and input light intensity. This linearity is indicative of photoconduction dominance, as opposed to thermal effects, which would typically display a nonlinear behavior due to the exponential relationship between temperature and carrier concentration.

Figure 4(d) illustrates the time response of the photoconduction current at negative bias, measured using a chopper and oscilloscope. The observed rise and fall times are approximately 2 μs, which is significantly faster than most conventional photodiodes. This result may be influenced by the preamplifier used during measurement, which could introduce additional parasitic capacitance, suggesting that the actual response time may be even shorter. Notably, a previous study reported a heterostructure device with a photoresponse time below 15 μs and a rectification ratio of approximately 60 at zero gate bias [3]. In comparison, our device demonstrates a faster response time of 2 μs and a significantly higher rectification ratio of 10^3 at zero gate bias. This improvement is likely due to the reduced size of the material, which requires fewer photons to generate current and thus demands only a short relaxation time. Additionally, the precise control over the CNT-MoS_2 interface in our inkjet-printed device reduces defects and enhances charge transport efficiency. This characteristic indicates that our device is well-suited for high-frequency applications and offers the advantage of size control for tailored performance.

4 Conclusions

In this study, we successfully demonstrated the fabrication and

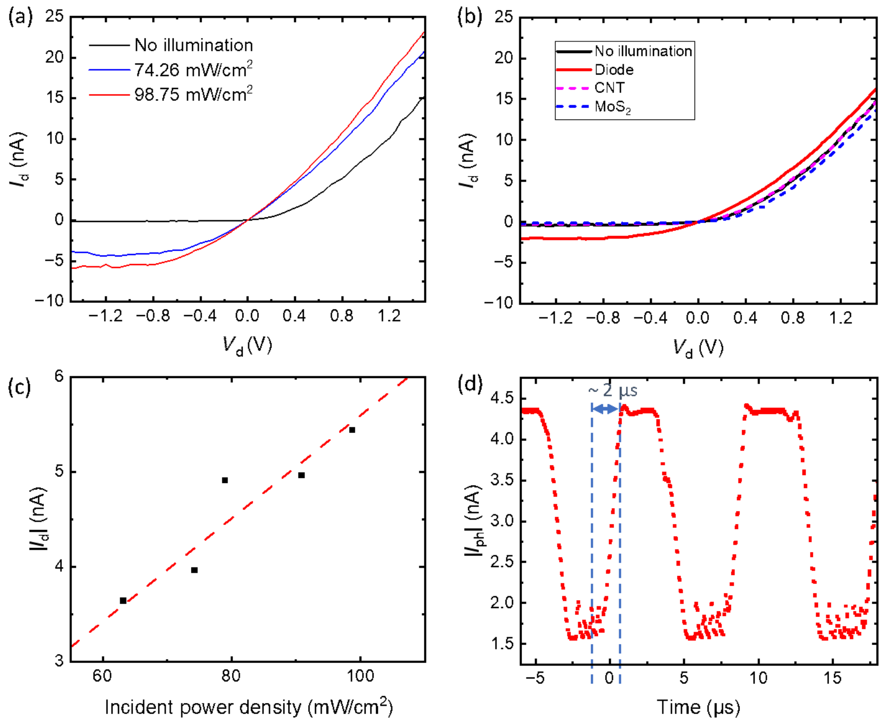

Figure 4 Photoconduction characterization and response time of the heterojunction diode. (a) Photocurrent measurement of the heterojunction diode at zero gate bias under illumination from a solar simulator, showing a pronounced photocurrent in the negative bias region, indicating potential for use as a photodetector. (b) Photocurrent response was measured using a 635 nm red laser beam with an intensity of approximately 21.66 mW/cm^2, focused on different regions of the device. No significant photoresponse is observed when the beam is focused on either the CNT or MoS_2 regions alone, confirming that the photoconduction current originates from the junction area. (c) Power dependence measurement under uniform solar simulator illumination, showing a linear relationship in the negative bias region, consistent with the linear relationship between photocurrent and input light intensity, thus confirming the dominance of photoconduction. (d) Time response of the photoconduction current at negative bias, measured using a chopper and oscilloscope. The rise and fall times are approximately 2 µs, which is faster than most conventional photodiodes.

characterization of an inkjet-printed CNT-MoS_2 heterojunction p-n diode, achieving a rectification ratio exceeding 10^3 at zero gate bias. Photoconduction measurements showed significant photocurrent under global illumination, confirming the device's potential as a photodetector. The rapid rise and fall times of approximately 2 µs indicate suitability for high-frequency applications. The use of inkjet printing technology allowed for precise, scalable, and cost-effective fabrication, simplifying the manufacturing process and enhancing the device's functional properties. These findings highlight the promise of inkjet-printed CNT-MoS_2 heterojunctions for advanced electronic and optoelectronic systems, paving the way for further research and development in this area. This work underscores the potential for innovative, low-cost solutions in the production of sophisticated electronic devices, demonstrating the effectiveness of inkjet printing for future technological advancements.

Electronic Supplementary Material: Supplementary material (SEM image for the heterojunction device, hysteresis property of heterojunction I_{ds}–V_g sweep, hysteresis property of CNT/MoS_2, I_{ds}–V_g sweep, full map of incident power sweep of photoconduction measurement) is available in the online version of this article at https://doi.org/10.26599/NR.2025.94907059.

Data availability

All data needed to support the conclusions in the paper are presented in the manuscript and the Electronic Supplementary Material. Additional data related to this paper may be requested from the corresponding author upon request.

Acknowledgements

Authors acknowledge the support of this research by King Abdulaziz City for Science and Technology (KACST) through the Center of Excellence for Nanotechnologies (CEGN) under contract number 20132944.

Declaration of competing interest

All the contributing authors report no conflict of interests in this work. Author Chongwu Zhou is the editorial board member of this journal, but he is not involved in the peer-review or decision of this article.

Author contribution statement

F. G. T.: Conceptualization, data curation, investigation, validation, writing – original draft, writing – review & editing, experimental design. D. Z. C.: Investigation, data curation, experimental design. M. R. C.: Investigation, resources. Z. Y. Z.: Investigation, data curation. W. B. C.: Investigation, data curation, experimental design. Z. K. W.: Investigation, data curation. S. G.: Data curation. S. A. (Sarah Alsaggaf): Data curation. S. A. (Shahad Albawardi): Data curation. M. L. P.: Conceptualization. M. R. A.: Supervision, conceptualization, funding acquisition, writing – review & editing, experimental design. J. G. L.: Supervision, conceptualization, writing – review & editing, experimental design. C. W. Z.: Supervision, project administrationm, conceptualization, writing – review & editing, experimental design. All the authors have approved the final manuscript.

Use of AI statement

None.

References

[1] Feng, X. J.; Zhao, X.; Yang, L.; Li, M. Y.; Qie, F. X.; Guo, J. H.; Zhang, Y. C.; Li, T. H.; Yuan, W. X.; Yan, Y. All carbon materials p-n diode. *Nat. Commun.* **2018**, *9*, 3750.

[2] Galluzzo, A.; Melito, M.; Musumeci, S.; Saggio, M.; Raciti, A. A new high voltage power MOSFET for power conversion applications. In *Proceedings of 2000 IEEE Industry Applications Conference. Thirty-Fifth IAS Annual Meeting and World Conference on Industrial Applications of Electrical Energy*, Rome, Italy, 2000, pp 2966–2973.

[3] Jariwala, D.; Sangwan, V. K.; Wu, C. C.; Prabhumirashi, P. L.; Geier, M. L.; Marks, T. J.; Lauhon, L. J.; Hersam, M. C. Gate-tunable carbon nanotube-MoS_2 heterojunction p-n diode. *Proc. Natl. Acad. Sci. USA* **2013**, *110*, 18076–18080.

[4] Liu, X. H.; Mao, Y. L. p-type high-performance WSi_2N_4 MOSFETs with the ultrashort scale of sub-5 nm. *ACS Appl. Electron. Mater.* **2023**, *5*, 6716–6724.

[5] Xia, H.; Luo, M.; Wang, W. J.; Wang, H. L.; Li, T. X.; Wang, Z.; Xu, H. Y.; Chen, Y.; Zhou, Y.; Wang, F. et al. Pristine PN junction toward atomic layer devices. *Light Sci. Appl.* **2022**, *11*, 170.

[6] Jung, Y.; Li, X. K.; Rajan, N. K.; Taylor, A. D.; Reed, M. A. Record high efficiency single-walled carbon nanotube/silicon p-n junction solar cells. *Nano Lett.* **2013**, *13*, 95–99.

[7] Ji, P. R.; Yang, S. M.; Wang, Y.; Li, K. L.; Wang, Y. M.; Suo, H.; Woldu, Y. T.; Wang, X. M.; Wang, F.; Zhang, L. L. et al. High-performance photodetector based on an interface engineering-assisted graphene/silicon Schottky junction. *Microsyst. Nanoeng.* **2022**, *8*, 9.

[8] Zhang, M.; Zhang, F.; Wang, Y.; Zhu, L. J.; Hu, Y. F.; Lou, Z. D.; Hou, Y. B.; Teng, F. High-performance photodiode-type photodetectors based on polycrystalline formamidinium lead iodide perovskite thin films. *Sci. Rep.* **2018**, *8*, 11157.

[9] Wu, G.; Tang, L. B.; Deng, G. R.; Liu, L. N.; Hao, Q.; Yuan, S. Z.; Wang, J. Y.; Wei, H.; Zhao, Y. P.; Yue, B. et al. Transparent dual-band ultraviolet photodetector based on graphene/p-GaN/AlGaN heterojunction. *Opt. Express* **2022**, *30*, 21349–21361.

[10] Shen, C. F.; Liu, Y. H.; Wu, J. B.; Xu, C.; Cui, D. Z.; Li, Z.; Liu, Q. Z.; Li, Y. R.; Wang, Y. X.; Cao, X. et al. Tellurene photodetector with high gain and wide bandwidth. *ACS Nano* **2020**, *14*, 303–310.

[11] Mahmoodi, E.; Amiri, M. H.; Salimi, A.; Frisenda, R.; Flores, E.; Ares, J. R.; Ferrer, I. J.; Castellanos-Gomez, A.; Ghasemi, F. Paper-based broadband flexible photodetectors with van der Waals materials. *Sci. Rep.* **2022**, *12*, 12585.

[12] Pejović, V.; Lee, J.; Georgitzikis, E.; Li, Y. L.; Kim, J. H.; Lieberman, I.; Malinowski, P. E.; Heremans, P.; Cheyns, D. Thin-film photodetector optimization for high-performance short-wavelength infrared imaging. *IEEE Electron Device Lett.* **2021**, *42*, 1196–1199.

[13] Li, X.; Aftab, S.; Hussain, S.; Kabir, F.; Al-Sehemi, A. G.; Aslam, M.; Kim, J. H.; Goud, B. S. Progress in photodetector devices utilizing transition metal dichalcogenides. *J. Mater. Chem. C* **2024**, *12*, 1211–1232.

[14] Lv, Z. J.; He, G.; Qiu, C. F.; Fan, Y. Y.; Wang, H. Y.; Liu, Z. J. CMOS monolithic photodetector with a built-in 2-dimensional light direction sensor for laser diode based underwater wireless optical communications. *Opt. Express* **2021**, *29*, 16197–16204.

[15] Mallik, S. K.; Padhan, R.; Roy, S.; Sahu, M. C.; Sahoo, S.; Sahoo, S. Direct transfer of monolayer MoS_2 device arrays for potential applications in flexible electronics. *ACS Appl. Nano Mater.* **2024**, *7*, 4796–4804.

[16] Zhu, W. J.; Low, T.; Lee, Y. H.; Wang, H.; Farmer, D. B.; Kong, J.; Xia, F. N.; Avouris, P. Electronic transport and device prospects of monolayer molybdenum disulphide grown by chemical vapour deposition. *Nat. Commun.* **2014**, *5*, 3087.

[17] Sebastian, A.; Pendurthi, R.; Choudhury, T. H.; Redwing, J. M.; Das, S. Benchmarking monolayer MoS_2 and WS_2 field-effect transistors. *Nat. Commun.* **2021**, *12*, 693.

[18] Tsai, H. J.; Yang, Y. K.; Li, Y. C.; Yeh, J.; Chen, P. C.; Kuo, Y. H.; Hsu, W. K. Production of carbon nanotube paper-based thermoelectric devices with the peltier effect. *ACS Appl. Electron. Mater.* **2023**, *5*, 4445–4450.

[19] Li, Z.; Jinkins, K. R.; Cui, D. Z.; Chen, M. R.; Zhao, Z. Y.; Arnold, M. S.; Zhou, C. W. Air-stable n-type transistors based on assembled aligned carbon nanotube arrays and their application in complementary metal-oxide-semiconductor electronics. *Nano Res.* **2022**, *15*, 864–871.

[20] Huo, N. J.; Yang, Y. J.; Wu, Y. N.; Zhang, X. G.; Pantelides, S. T.; Konstantatos, G. High carrier mobility in monolayer CVD-grown MoS_2 through phonon suppression. *Nanoscale* **2018**, *10*, 15071–15077.

[21] Kim, T.; Fan, S. D.; Lee, S.; Joo, M. K.; Lee, Y. H. High-mobility junction field-effect transistor via graphene/MoS_2 heterointerface. *Sci. Rep.* **2020**, *10*, 13101.

[22] Das, S.; Lee, B. H.; Linstadt, R. T. H.; Cunha, K.; Li, Y. L.; Kaufman, Y.; Levine, Z. A.; Lipshutz, B. H.; Lins, R. D.; Shea, J. E. et al. Molecularly smooth self-assembled monolayer for high-mobility organic field-effect transistors. *Nano Lett.* **2016**, *16*, 6709–6715.

[23] Chen, M. R.; Zhang, A. Y.; Liu, Y. H.; Cui, D. Z.; Li, Z.; Chung, Y. H.; Mutyala, S. P.; Mecklenburg, M.; Nie, X.; Xu, C. et al. Gold-vapor-assisted chemical vapor deposition of aligned monolayer WSe_2 with large domain size and fast growth rate. *Nano Res.* **2020**, *13*, 2625–2631.

[24] Zub, K.; Hoeppener, S.; Schubert, U. S. Inkjet printing and 3D printing strategies for biosensing, analytical, and diagnostic applications. *Adv. Mater.* **2022**, *34*, 2105015.

[25] Singh, M.; Haverinen, H. M.; Dhagat, P.; Jabbour, G. E. Inkjet printing-process and its applications. *Adv. Mater.* **2010**, *22*, 673–685.

[26] Wang, H. L.; Dong, Y.; Fu, X.; Zhao, X. Z.; Zhao, Q. X.; Xia, M. J. Heterojunction infrared photodiodes with high dynamic range based on lead sulfide quantum dot and zinc oxide nanomembrane. *IEEE Trans. Nanotechnol.* **2023**, *22*, 359–364.

[27] Chen, M. R.; Cui, D. Z.; Wang, N.; Weng, S. Z.; Zhao, Z. Y.; Tian, F. G.; Gao, X. B.; He, K. M.; Chiang, C. T.; Albawardi, S. et al. Inkjet-printed MoS_2 nanoplates on flexible substrates for high-performance field effect transistors and gas sensing applications. *ACS Appl. Nano Mater.* **2023**, *6*, 3236–3244.

[28] Wen, D.; Wang, X.; Liu, L.; Hu, C.; Sun, C.; Wu, Y. R.; Zhao, Y. L.; Zhang, J. X.; Liu, X. D.; Ying, G. B. Inkjet printing transparent and conductive MXene ($Ti_3C_2T_x$) films: A strategy for flexible energy storage devices. *ACS Appl. Mater. Interfaces* **2021**, *13*, 17766–17780.

[29] Hayman, M.; McMenamin, K. J.; Jensen, J. B. Response time characteristics of the fast-2D optical array probe detector board. *J. Atmos. Ocean. Technol.* **2016**, *33*, 2569–2583.

[30] Wang, Y. F.; Zou, X. P.; Zhu, J. L.; Zhang, C. Q.; Cheng, J.; Wang, J. Q.; Wang, X. L.; Li, X. T.; Song, K. K.; Ren, B. K. et al. Investigation of the photoresponse and time-response characteristics of HDA-BiI_5-based photodetectors. *Materials* **2022**, *15*, 321.

[31] Wu, F.; Li, Q.; Wang, P.; Xia, H.; Wang, Z.; Wang, Y.; Luo, M.; Chen, L.; Chen, F. S.; Miao, J. S. et al. High efficiency and fast van der Waals hetero-photodiodes with a unilateral depletion region. *Nat. Commun.* **2019**, *10*, 4663.

[32] Pan, T.; Liu, S. H.; Zhang, L. T.; Xie, W. F. Flexible organic optoelectronic devices on paper. *iScience* **2022**, *25*, 103782.

[33] Tsai, C. H.; Lee, S. G.; Chen, C. K.; Hsu, C. H.; Lee, C. S.; Shen, K. Y.; Cheng, S. C.; Lee, C. H.; Cheng, F. Y.; Huang, M. F. et al. Low-cost and highly reliable optoelectronic devices for 10-Gb/s Ethernet applications. In *Proceedings of SPIE 5595, Active and Passive Optical Components for WDM Communications IV*, Philadelphia, Pennsylvania, United States, 2004, pp 371–382.

[34] Lowry, M.; Lu, S. Y.; Pocha, M.; Strand, O. T. Low-cost packaging of high-performance optoelectronic components. In *Proceedings of the Integrated Photonics Research*, Dana Point, California United States, 1995, pp IThE3.

[35] Zhang, C.; Tan, J. Y.; Pan, Y. K.; Cai, X. K.; Zou, X. L.; Cheng, H. M.; Liu, B. L. Mass production of 2D materials by intermediate-assisted grinding exfoliation. *Natl. Sci. Rev.* **2020**, *7*, 324–332.

[36] Zhang, C.; Luo, Y. T.; Tan, J. Y.; Yu, Q. M.; Yang, F. N.; Zhang, Z. Y.; Yang, L. S.; Cheng, H. M.; Liu, B. L. High-throughput production of cheap mineral-based two-dimensional electrocatalysts for high-current-density hydrogen evolution. *Nat. Commun.* **2020**, *11*, 3724.

[37] Sangwan, V. K.; Beck, M. E.; Henning, A.; Luo, J. J.; Bergeron, H.; Kang, J. M.; Balla, I.; Inbar, H.; Lauhon, L. J.; Hersam, M. C. Self-aligned van der Waals heterojunction diodes and transistors. *Nano Lett.* **2018**, *18*, 1421–1427.

[38] Kim, B. H.; Kang, J. W. Electroluminescent MgZnO/ZnO heterojunction diode. *Appl. Sci. Converg. Technol.* **2023**, *32*, 151–154.

[39] Yan, R. S.; Fathipour, S.; Han, Y. M.; Song, B.; Xiao, S. D.; Li, M. D.; Ma, N.; Protasenko, V.; Muller, D. A.; Jena, D. et al. Esaki diodes in van der Waals heterojunctions with broken-gap energy band alignment. *Nano Lett.* **2015**, *15*, 5791–5798.

[40] Chen, Y.; Wang, X. D.; Huang, L.; Wang, X. T.; Jiang, W.; Wang, Z.; Wang, P.; Wu, B. M.; Lin, T.; Shen, H. et al. Ferroelectric-tuned van der Waals heterojunction with band alignment evolution. *Nat. Commun.* **2021**, *12*, 4030.

[41] Maheswaran, R.; Shanmugavel, B. P. A critical review of the role of carbon nanotubes in the progress of next-generation electronic applications. *J. Electron. Mater.* **2022**, *51*, 2786–2800.

[42] Lee, D. K.; Yoo, J.; Kim, H.; Kang, B. H.; Park, S. H. Electrical and thermal properties of carbon nanotube polymer composites with various aspect ratios. *Materials* **2022**, *15*, 1356.

[43] Cheng, Z. F.; He, S. D.; Han, X. N.; Zhang, X. D.; Chen, L. N.; Duan, S. J.; Zhang, S. M.; Xia, M. G. Improving electron mobility in MoS_2 field-effect transistors by optimizing the interface contact and enhancing the channel conductance through local structural phase transition. *J. Mater. Chem. C* **2024**, *12*, 2794–2802.

[44] Ji, L. P.; Shi, J.; Zhang, Z. Y.; Wang, J.; Zhang, J. C.; Tao, C. L.; Cao, H. N. Theoretical prediction of high electron mobility in multilayer MoS_2 heterostructured with $MoSe_2$. *J. Chem. Phys.* **2018**, *148*, 014704.

[45] Jorio, A.; Saito, R. Raman spectroscopy for carbon nanotube applications. *J. Appl. Phys.* **2021**, *129*, 021102.

[46] Yang, M. M.; Liu, Y.; Cong, R. D.; Zhang, Y.; Zhang, Y. F.; Tan, L.; Hu, X. W.; Wu, C. L.; Liu, Y. L.; Dang, W. et al. Angle-resolved polarized Raman spectra of linear MoS_2 nanostructures for optical anisotropy detection. *ACS Appl. Nano Mater.* **2023**, *6*, 11299–11308.

[47] Kang, D. H.; Park, N.; Ko, J. H.; Bae, E.; Park, W. Oxygen-induced p-type doping of a long individual single-walled carbon nanotube. *Nanotechnology* **2005**, *16*, 1048–1052.

[48] Park, Y.; Li, N. N.; Jung, D.; Singh, L. T.; Baik, J.; Lee, E.; Oh, D.; Kim, Y. D.; Lee, J. Y.; Woo, J. et al. Unveiling the origin of n-type doping of natural MoS_2: Carbon. *npj 2D Mater. Appl.* **2023**, *7*, 60.

[49] Meng, Y.; Wang, W. J.; Wang, W.; Li, B. W.; Zhang, Y. X.; Ho, J. Anti-ambipolar heterojunctions: Materials, devices, and circuits. *Adv. Mater.* **2024**, *36*, 2306290.

[50] Lv, Y. H.; Wu, C. Y.; Zhao, Y.; Wu, G.; Abid, M.; Cho, J.; Choi, M.; Coileáin, Ó. C.; Hung, K. M.; Chang, C. R. et al. Robust anti-ambipolar behavior and gate-tunable rectifying effect in van der Waals p-n junctions. *ACS Appl. Electron. Mater.* **2022**, *4*, 5487–5497.

[51] Li, X.; Carey, J. E.; Sickler, J. W.; Pralle, M. U.; Palsule, C.; Vineis, C. J. Silicon photodiodes with high photoconductive gain at room temperature. *Opt. Express* **2012**, *20*, 5518–5523.